The severe acute respiratory syndrome-coronavirus replicative protein nsp9 is a single-stranded RNA-binding subunit unique in the RNA virus world

Marie-Pierre Egloff*, François Ferron*, Valérie Campanacci*, Sonia Longhi*, Corinne Rancurel*, Hélène Dutartre*, Eric J. Snijder†, Alexander E. Gorbalenya†, Christian Cambillau*‡, and Bruno Canard*‡

*Architecture et Fonction des Macromolécules Biologiques, Unité Mixte de Recherche 6098 Centre National de la Recherche Scientifique and Universités Aix-Marseille I et II, 31 Chemin Joseph Aiguier, 13402 Marseille Cedex 20, France; and †Molecular Virology Laboratory, Department of Medical Microbiology, Center of Infectious Diseases, Leiden University Medical Center, P.O. Box 9600, 2300 RC, Leiden, The Netherlands

Edited by Stephen C. Harrison, Harvard Medical School, Boston, MA, and approved January 28, 2004 (received for review November 26, 2003)

The recently identified etiological agent of the severe acute respiratory syndrome (SARS) belongs to *Coronaviridae* (CoV), a family of viruses replicating by a poorly understood mechanism. Here, we report the crystal structure at 2.7-Å resolution of nsp9, a hitherto uncharacterized subunit of the SARS-CoV replicative polyproteins. We show that SARS-CoV nsp9 is a single-stranded RNA-binding protein displaying a previously unreported, oligosaccharide/oligonucleotide fold-like fold. The presence of this type of protein has not been detected in the replicative complexes of RNA viruses, and its presence may reflect the unique and complex CoV viral replication/transcription machinery.

In 2003, a human coronavirus (CoV) was identified as the causative agent of a form of atypical pneumonia: severe acute respiratory syndrome-CoV (SARS-CoV) (1–5). *Coronaviridae* have the longest known single-stranded (ss)RNA genome (27–31.5 kb), with a complex genetic organization and sophisticated replication/transcription cycle (6, 7). Twenty-eight proteins are predicted to be encoded by the SARS-CoV genome (8, 9). The nonstructural (nsp) or "replicase" proteins of CoVs are derived from an unusually large replicase gene of >20 kb that consists of two large ORFs (ORFs 1a and 1b). Translation of this replicase gene from the incoming genomic RNA is the first step in CoV genome expression and includes a −1 ribosomal frameshift to express the ORF1b-encoded polypeptide. Translation products are the pp1a polyprotein (>4,000 amino acids) and the C-terminally extended pp1ab polyprotein (>7,000 amino acids), which are both cleaved by two or three ORF1a-encoded viral proteinases (10). Most of these replicase cleavage products assemble into a membrane-associated viral replication/transcription complex. Among other components, this complex includes a set of relatively small polypeptides (nsp6 to nsp11) encoded by the 3′ region of ORF1a, for which no predicted nor proven function has been assigned. For the mouse hepatitis CoV, several of these cleavage products were reported to colocalize with other components of the viral replication complex in the perinuclear region of the infected cell (11), suggesting their involvement (directly or indirectly) in viral RNA metabolism.

As part of a viral structural genomics program (12), we have cloned the 28 gene products of SARS-CoV and expressed them either as full-length proteins or as (predicted) functional domains. The determination of the three-dimensional structures of these gene products is expected to facilitate and accelerate discovery of drugs against this emerging and life-threatening pathogen. Furthermore, structural homology search is becoming a powerful method to infer biochemical and/or biological function of previously uncharacterized proteins. We report here the crystal structure of nsp9, one the SARS-CoV uncharacterized nonstructural protein, as well as evidence for its function as an ssDNA/RNA-binding protein.

Materials and Methods

Crystallization, Structure Determination, and Refinement. SARS-CoV nsp9 has been expressed, purified, and crystallized as described (12). X-ray diffraction data were collected at 100 K at the European Synchrotron Radiation Facility, Grenoble, France. Native data were collected on beamline ID14–1 by using a Quantum ADSC Q4R charge-coupled device detector. Crystals diffracted X-rays to 2.7-Å resolution and belonged to space group $P6_122$ with unit cell dimensions $a = b = 89.7$ Å, $c = 136.7$ Å. There are two molecules per asymmetric unit, leading to a solvent content of ≈60%. The structure was solved by using single-wavelength anomalous dispersion data (13) collected at the peak wavelength of selenium on beamline ID14–4.

Data were integrated with MOSFLM and were scaled by using SCALA (14). The four expected selenium sites (two in each of the two molecules of the asymmetric unit) were identified and refined by using SOLVE (15). Density modification of the experimental maps and initial fragment building was performed with RESOLVE (16). Model building was carried out by using TURBO-FRODO (17) and maximum-likelihood refinement was performed with REFMAC5 (18) using NCS restraints. Residues 3–113 could be modeled and refined in molecule A, and residues 4–113 in molecule B. Four sulfate ions and 31 water molecules were added manually during refinement. Overall geometric quality of the model was assessed by using PROCHECK (19). A total of 86.1% of the residues were found in the most favored regions of the Ramachandran plot, and 13.4% were in additionally allowed regions. The solvent-accessible surface of nsp9 was calculated and displayed by using GRASP (20) and SWISS-PDBVIEWER (21). Fig. 1 *A* and *B* was generated by using MOLSCRIPT (22) and was rendered by using RASTER3D (23). The alignment of Fig. 1*C* has been displayed by using the program ESPRIPT (24).

Surface Plasmon Resonance and Fluorescence Spectroscopy. DNA and RNA oligonucleotides were purchased from Life Technologies (Grand Island, NY) and Amersham Pharmacia, respectively. Surface plasmon resonance measurements were performed on a BIAcore apparatus (Pharmacia Biosensor) by using the BIAlogue kinetics evaluation program (BIAEVALUATION V.3.1, Pharmacia Biosensor). Biotinylated oligonucleotides were

This paper was submitted directly (Track II) to the PNAS office.

Abbreviations: SARS, severe acute respiratory syndrome; CoV, coronavirus; ss, single-stranded; SSB, ssDNA-binding protein; OB, oligosaccharide/oligonucleotide-binding; K_{Dapp}, dissociation equilibrium constant; NCBI, National Center for Biotechnology Information.

Data deposition: The atomic coordinates and structure factors have been deposited in the Protein Data Bank, www.pdb.org (PDB ID code 1QZ8).

‡To whom correspondence should be addressed. E-mail: cambillau@afmb.cnrs-mrs.fr or bruno@afmb.cnrs-mrs.fr.

www.pnas.org/cgi/doi/10.1073/pnas.0307877101

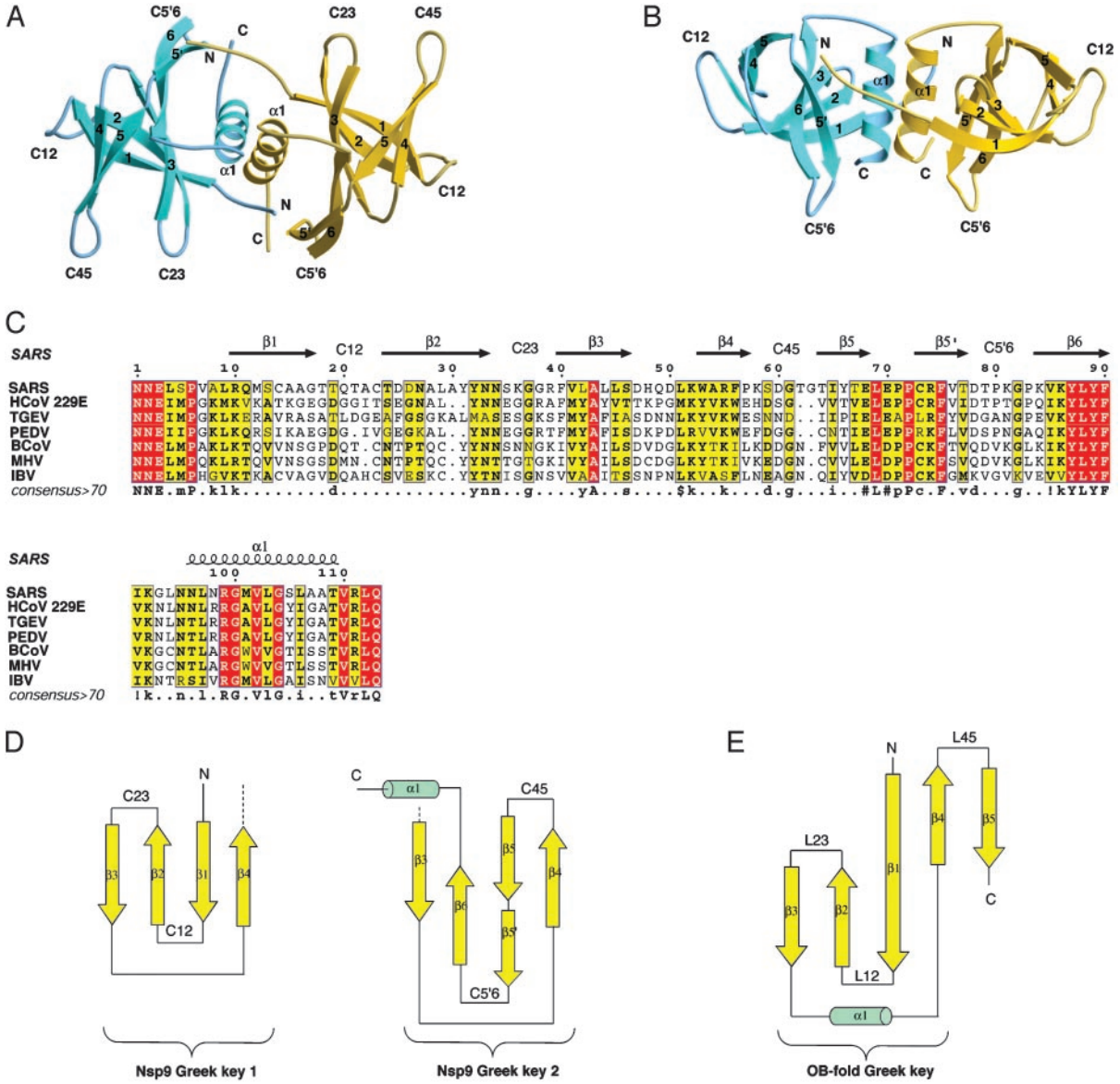

Fig. 1. Crystal structure, sequence, and topology of SARS-CoV nsp9. (*A*) Ribbon representation of SARS-CoV nsp9. One molecule of the dimer is gold and the other is cyan. Loops between strands x and y are labeled C. (*B*) A 90° view of *A*. (*C*) Multiple alignment of nsp9 sequences from SARS-CoV National Center for Biotechnology Information (NCBI) accession no. AY291315, and several related CoVs: HCoV 229E, human CoV 229E, NCBI accession no. NP_073550; TGEV, transmissible gastroenteritis virus, NCBI accession no. NP_058423; PEDV, porcine epidemic diarrhea virus CV777, NCBI accession no. NP_598309, BCoV, bovine CoV, NCBI accession no. NP_150074; MHV, mouse hepatitis virus MHV-A59, NCBI accession no. NP_045298; and IBV, avian infectious bronchitis virus, NCBI accession no. NP_040829). The consensus sequence (identity cutoff >70%) is displayed under the multiple sequence alignment. Dots and residues in lowercase correspond to positions for which the residue conservation is under and above the cutoff value, respectively; positions marked by # correspond to either Asn, Asp, Glu, or Gln; positions marked by ! correspond to either Ile or Val, and $ corresponds to Leu or Met. Residues that are conserved in all sequences are boxed in red, and those for which conservation is >70% are boxed in yellow. For a given position, only residues homologous to the consensus are bold. The top numbers correspond to the amino acid sequence of SARS-CoV nsp9. Secondary structure elements and loops of nsp9 SARS-CoV are numbered according to Fig. 1 and are indicated above the alignment. (*D*) Schematic representation of nsp9 topology. nsp9 SARS-CoV β-barrel structure is a concatenation of two Greek key motifs, Greek key 1 having a g− topology and Greek key 2 a g+ topology (30), resulting in a six-stranded RH-g− to g+ topology. β-strands and α-helices are symbolized by arrows and cylinders, respectively, and they are numbered consistently with the sequence alignment. (*E*) Schematic representation of the typical Greek key (g− topology) motif found in the OB fold.

immobilized on a Sensor Chip SA according to the manufacturer's instructions (BIAcore).

Fluorescence quenching of the single tryptophan in nsp9 was measured by using a Cary Eclipse (Varian) equipped with a front-face fluorescence accessory at 20°C, by using 2.5-nm excitation and 10-nm emission bandwidths. The excitation wavelength was 280 nm and the emission spectra were measured between 290 and 540 nm. Titrations were performed in a 1-ml quartz fluorescence cuvette containing 1 μM protein in 10 mM Tris·HCl buffer/300 mM NaCl, pH 8.0, and by the successive addition of aliquots of appropriate nucleic acids stock solutions (1 mM). Experimental fluorescence intensities were corrected for dilution. Data were analyzed by plotting the relative fluorescence intensities at 340 nm at increasing concentrations of quencher. Dissociation equilibrium constant (K_{Dapp}) values were determined from data fitted to a single exponential equation, by

Table 1. Summary of crystallographic data

	SeMet	Native
Data collection		
Wavelength, Å	0.9793	0.9340
Resolution range, Å†	30–3.0 (3.11–3.0)	3.0–2.7 (2.84–2.7)
No. of unique reflections	6,831	9,345
No. of measured reflections	97,058	100,668
$I/\sigma I$	7.4 (6)	9.4 (1.6)
Multiplicity	14.2 (14.2)	10.8 (10.2)
Completeness, %	99.9 (99.9 anomalous)	99.1 (99.0)
R_{merge}*, %	8.4 (47.9)	5.6 (43.3)
Refinement		
Resolution limits, Å		15.0–2.7
R factor†, R_{free}‡, %		23.4/27.1
rms deviation: bonds, Å/angles, °		0.018/1.88

SeMet, selenomethionyl single-wavelength anomalous dispersion data set. Values in parentheses are for the highest-resolution shell.
*R_{merge}, $\Sigma\Sigma i\ |Ih - Ii|/\Sigma\Sigma Ih$, where Ih is the mean intensity for reflection h.
†R factor, $\Sigma||F_o| - |F_c||/\Sigma\ |F_o|$, where F_o and F_c are measured and calculated structure factors, respectively.
‡R_{free} was calculated over 5% of reflections not used in the refinement.

using the PRISM 3.02 nonlinear regression tool (GraphPad, San Diego).

Results and Discussion

The crystal structure of SARS-CoV nsp9 is reported (Fig. 1 and Table 1). Crystals contain a dimer in the asymmetric unit (Fig. 1 *A* and *B*); in each monomer, seven β-strands and one α-helix (Fig. 1 *A–C*) are arranged into a single compact domain and form a cone-shaped β-barrel flanked by the C-terminal α-helix. The latter makes a 45° angle with the axis of the β-barrel and has a high content of hydrophobic residues, yielding two hydrophobic sides. One faces the β-barrel and the other interacts with the α-helix of the second crystallographic monomer (Fig. 1 *A* and *B*). This dimer is therefore assembled by hydrophobic interactions and is further stabilized by four long hydrogen bonds involving main-chain atoms. Comparing the buried dimerization surface of 1,632 Å^2 with the few other crystallographic contacts suggests that this crystallographic dimer is also present in solution, which is in agreement with dynamic light scattering and gel permeation experiments (12). This surface of 1,632 Å^2 is among standard interfacial areas found in biologically relevant dimers (25). The two molecules of the dimer are spatially similar (rms deviations value of 0.99 Å over the 109 C^α atoms of the structure). This deviation is further reduced after exclusion of N and C termini together with the tips of three long loops (L23, L45, and L5′6) emerging from the barrel (Fig. 1*A*, rms deviation of 0.45 Å over the 87 C^α atoms).

Screening public protein databases with BLAST or PSI-BLAST (26) failed to identify any sequence homologue of CoV nsp9 proteins, which is consistent with their yet unknown function. No structural homologues of nsp9 were found when scanning either the Protein Data Bank with the DALI server (27) or the CATH database (28) with the GRATH server. Visual inspection of the Structural Classification of Protein database, version 1.63 (29), revealed some common features between SARS-CoV nsp9 and four different existing folds (trypsin-like proteases, the C-terminal domain of μ-transposase, α- and β-subunits of F1-ATP synthase-like, and small protein B). Only the N-terminal six-stranded β-barrel of the trypsin-like proteases displays the same connectivity and spatial arrangement as nsp9 monomers, and can be significantly superimposed [rms deviation of 1.73 Å over the

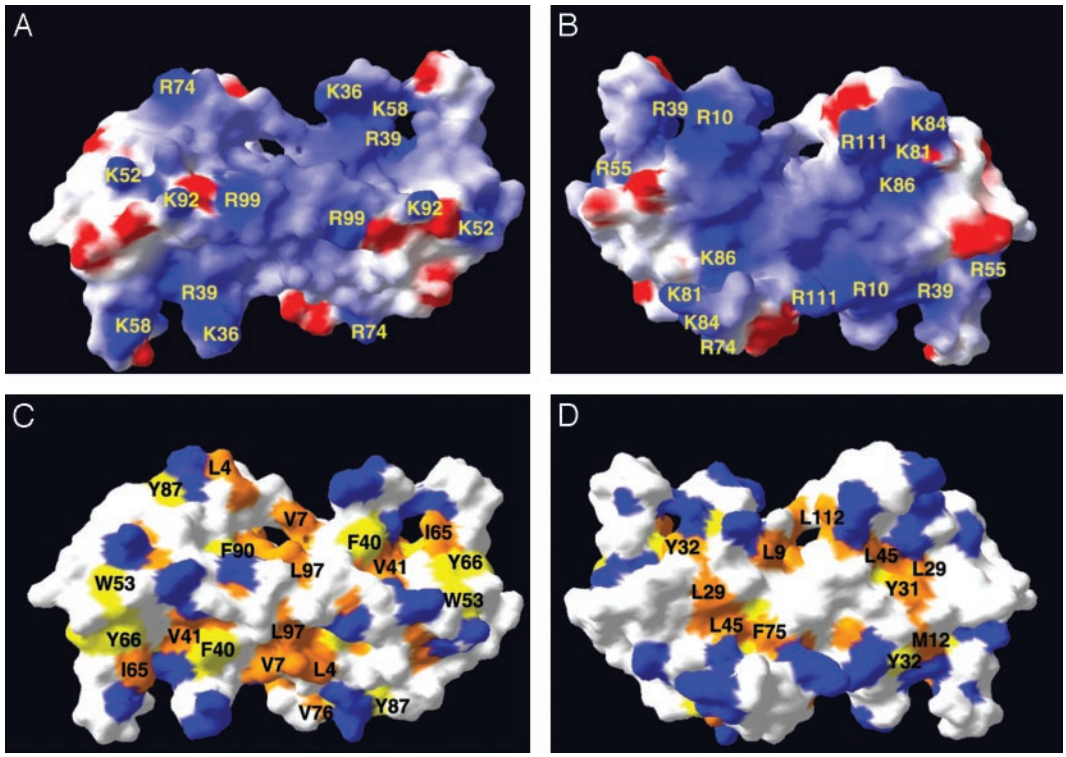

Fig. 2. Surface analysis of SARS-CoV nsp9. (*A*) Electrostatic surface potential of nsp9 viewed from the same orientation as in Fig. 1*A*. Potential values range from −5 kT (red) to 0 (white) and to +5 kT (blue), where k is the Boltzman constant and T is the temperature. Accessible Lys and Arg residues are indicated. (*B*) Back view from *A*, with the same color code. (*C*) Accessible surface colored according to the following: Lys or Arg are blue; Tyr, Phe, and Trp are yellow; and Val, Leu, and Ile are orange. The orientation is the same than in *A*. (*D*) Same coloring as in *C* with the same orientation as in *B*.

74 C^{α} atoms when superimposing nsp9 and thrombin structure (PDB code 1A2C)]. This homology has no functional relevance, however, because nsp9 lacks a trypsin-like catalytic triad. This visual inspection did, however, reveal two other interesting features. First, six-stranded closed β-barrels have been identified in several proteins that interact with RNA, such as the small protein B (30) and the domain III of EF-Tu (31). Second, the short six-stranded β-barrel of nsp9 includes an opened five-stranded barrel reminiscent of the five-stranded β-barrel of the oligosaccharide/oligonucleotide-binding (OB)-fold proteins. The latter proteins form a superfamily in which two-thirds of the members are nucleic acid-binding proteins (32).

Structural homology between nsp9 and small protein B (or domain III of EF-Tu) is not strong enough to allow a reliable superimposition, which would have provided an indication about the localization of a putative nucleic acid-binding site. Likewise, nsp9 and OB-fold proteins cannot easily be compared, because Greek key 1 of nsp9 (Fig. 1*D*) and the classical OB-fold Greek key motif (Fig. 1*E*) cannot be superimposed. Although there is a structural equivalence between the Greek key 2 motif of nsp9 (Fig. 1*D*) and the OB-fold Greek key, the connectivity between strands is different. When both motifs are superimposed, the canonical binding face observed in the OB fold is buried in the dimer interface of nsp9. For these reasons, nsp9 may be considered as a new variant within the OB superfamily. Nonetheless, nsp9 displays the same features that OB-fold proteins use to bind nucleic acids: a network of positively charged amino acids defines a positive track suitable for binding the phosphate backbone to the protein surface (Fig. 2 *A* and *B*), whereas exposed aromatic residues might provide stacking interactions with nucleobases (Fig. 2 *C* and *D*). These residues are conserved in all CoV nsp9 sequences (Arg-10, Lys-52, Trp-53, Arg-55, Arg-74, Phe-75, Lys-86, Tyr-87, Phe-90, Lys-92, Arg-99, and Arg-111 in Figs. 1*C* and 2 *A–D*), further suggesting that nsp9 is a nucleic acid-binding protein. In addition, two extended loops L23 and L45 display weak electron density associated with high *B* factor values, indicating that they are flexible and/or mobile. They line the positively charged track, and they may clamp nucleic acids on the nsp9 surface after conformational change, as observed in other OB-fold proteins (32). In other members of the OB-fold superfamily, each monomer has its own, autonomous single-stranded nucleic acid-binding site. For example, replication protein A trimerizes by means of its C-terminal α-helix, each monomer keeping an individual ssDNA-binding site acting cooperatively with other units of the trimer (33, 34). In nsp9, it is the dimeric form that provides a single, uninterrupted nucleic acid-binding site.

Surface plasmon resonance was used to demonstrate the function of nsp9 as a nucleic acid-binding protein. Biotinylated oligonucleotides bound to a streptavidin-coated solid support are able to bind nsp9 (Fig. 3*A*). This function was confirmed by fluorescence experiments. As a fluorophore, nsp9 monomer has a single Trp residue (Trp-53), which is partially exposed to the solvent. The Trp-53 indole moiety is in a polar environment comprising side chains of Gln-20, Gly-66, and more remotely, Lys-52. Interactions of Trp-53 with ligand might therefore quench its fluorescence. This occurrence was indeed observed by using ssDNA and ssRNA oligonucleotides of defined sequence. The quenching efficiency increased steadily when the probe size was increased from 6-mer to 45-mer and then reached a plateau (Fig. 3*B*). The occurrence of this plateau suggests that the nsp9 tryptophans in the dimer achieve an optimal energy transfer (reflecting optimal molecular interactions) only through the tight packing of probes equal or longer than the 45-mer. In contrast, shorter probes do not result in optimal transfer, probably due to remote or loose contacts with the tryptophans. With both ssDNA and ssRNA, a large decrease in tryptophan fluorescence was observed (Fig. 3*C*), but the emission maximum

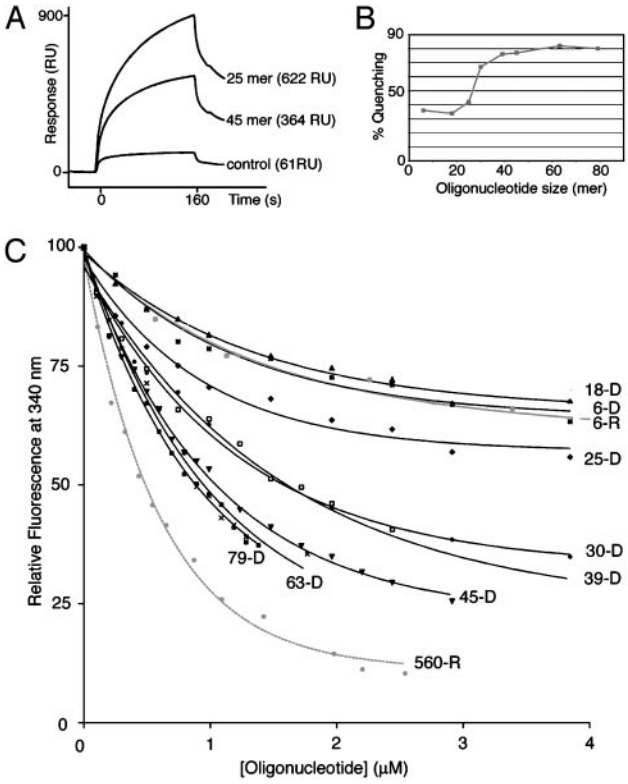

Fig. 3. SARS-CoV nsp9 is an oligonucleotide-binding protein. (*A*) BIAcore analysis of nsp9 binding to immobilized DNA oligonucleotides. The protein (16 μM) was injected at a flow rate of 5 μl/min in HBS buffer on dextran layers containing 550 and 850 resonance units (RU) of the 25- and 45-mer oligonucleotides, respectively. The sensorgrams are the result of two independent experiments. RU values at 125 s (5 s after the end of the injection) are indicated. (*B*) Tryptophan fluorescence quenching study on SARS-CoV nsp9. The tryptophan fluorescence quenching at the plateau (in percent) is plotted versus the length of ssDNA probes. The K_{Dapp} values are extracted from the plot displayed in *C* and are discussed in the text. (*C*) The relative fluorescence of nsp9 at 340 nm is plotted as a function of the oligonucleotide concentration for ssDNA, ranging from 6- to 79-mer and for a 6, and 560-mer ssRNA. D, DNA; R, RNA. The K_{Dapp} values (discussed in the text), result from the fitting of the data to a single exponential (GraphPad).

wavelength was unchanged, indicating (*i*) that the interaction is nonspecific and may involve the sugar-phosphate backbone rather than the bases, and (*ii*) that the environment of Trp-53 remains polar. The apparent affinity does not depend on the ssDNA length, because K_{Dapp} values fall between 0.63 and 1.1 μM when data are fitted to a single exponential (Fig. 3*C*). The strongest quenching (90%) and the best K_{Dapp} (0.4 μM) are observed with the 560-mer ssRNA, suggesting that each ssRNA binds several nsp9 dimers and that each nsp9 dimer can bind two distinct single-stranded segments.

The binding of both ssDNA and ssRNA of unrelated defined sequences, together with K_{Dapp} values in the micromolar range, suggests that the nucleic acid-binding activity of nsp9 is not sequence-specific. Much like the human CoV 229E helicase, which has RNA and DNA duplex-unwinding activities (35), nsp9 is able to bind ssDNA or ssRNA equally, although binding of the latter is expected to be the native function. In the infected cell, the coupling/compartimentation of the viral RNA synthesis with the RNA-binding function of nsp9 might render RNA versus DNA specificity unnecessary. The wrapping of ssRNA around the nsp9 dimer is an interesting possibility that is compatible with the structural characteristics of the nsp9 dimer described here. An ssRNA binding-function of nsp9 is also consistent with its

natural abundance in the replication complex. Due to a ribosomal frameshifting mechanism (36), nsp9 and other ORF1a-encoded CoV replicase subunits are produced in 3- to 5-fold excess relative to the "core" replicative enzymes [such as the RNA-dependent RNA polymerase and helicase (9) produced from replicase ORF1b]. For example, nsp9 might stabilize nascent nucleic acid during replication or transcription, thus providing protection from nucleases. The amount of nsp9 may not be enough to cover the entire ssRNA genome. The latter may not be entirely single-stranded, however, due to secondary RNA structure. Whether the ssRNA-binding function of nsp9 may be restricted to specific segments of the genome, or be complemented with other proteins is still an open question.

The complexity of the RNA synthesis machinery of CoVs has long been predicted, considering the size of the pp1a- and pp1ab-replicative polyproteins and the number of cleavage products produced from these precursors. Recently, Snijder *et al.* (8) described a set of putative RNA processing enzymes in the replicase complex of CoVs, including SARS-CoV. In addition to mere RNA replication, nsp9 could also participate in such a base-pairing-driven process as RNA processing. An informative parallel in the virus world is observed with bacteriophage T7: its gene 2.5 ssDNA-binding protein binds substrates with similar affinity as SARS-CoV nsp9 does [k_d in the μM range (37)] and is involved in replication/recombination/homologous base-pairing events (38, 39). The structural and functional characterization of nsp9 may also be relevant to SARS-CoV control: the SARS epidemics as well as previous work on CoVs have shown that genome plasticity (evolution by mutation and recombination) relate to pathogenicity and probably also to drug resistance. Because many viral and cellular single-stranded nucleic acid-binding proteins are essential (40), nsp9 is to be added to the list of potential targets for anti-CoV drug design.

We thank the staff at the European Synchrotron Radiation Facility for technical assistance and, in particular, Joanne Mac Carthy and Edward Mitchell for their assistance with data collection; Laurent Gauthier, Aurelia Salomoni, Cécile Durousseau, Fabienne Tocque, Nicolas Brémond, Willy Spaan, Peter Bredenbeek, Jessika Dobbe, and Sylvie Doublié for their contribution to this work; and Holli Conway for correcting the English. This work was supported by the Structural Proteomics in Europe project of the European Union 5th framework research program (Grant QLRT-2001-00988), by the French Genopole program, and by the Conseil Général des Bouches-du-Rhône.

1. Drosten, C., Gunther, S., Preiser, W., van der Werf, S., Brodt, H. R., Becker, S., Rabenau, H., Panning, M., Kolesnikova, L., Fouchier, R. A., *et al.* (2003) *N. Engl. J. Med.* **348,** 1967–1976.
2. Ksiazek, T. G., Erdman, D., Goldsmith, C. S., Zaki, S. R., Peret, T., Emery, S., Tong, S., Urbani, C., Comer, J. A., Lim, W., *et al.* (2003) *N. Engl. J. Med.* **348,** 1953–1966.
3. Marra, M. A., Jones, S. J., Astell, C. R., Holt, R. A., Brooks-Wilson, A., Butterfield, Y. S., Khattra, J., Asano, J. K., Barber, S. A., Chan, S. Y., *et al.* (2003) *Science* **300,** 1399–1404.
4. Peiris, J. S., Lai, S. T., Poon, L. L., Guan, Y., Yam, L. Y., Lim, W., Nicholls, J., Yee, W. K., Yan, W. W., Cheung, M. T., *et al.* (2003) *Lancet* **361,** 1319–1325.
5. Rota, P. A., Oberste, M. S., Monroe, S. S., Nix, W. A., Campagnoli, R., Icenogle, J. P., Penaranda, S., Bankamp, B., Maher, K., Chen, M. H., *et al.* (2003) *Science* **300,** 1394–1399.
6. Siddell, S. G. (1995) *The Coronaviridae* (Plenum, New York).
7. Lai, M. M. C. & Holmes, K. V. (2001) in *Fields Virology*, eds. Knipe, D. M. & Howley, P. M. (Lippincott, Williams & Wilkins, Philadelphia), Vol. 1, pp. 1163–1185.
8. Snijder, E. J., Bredenbeek, P. J., Dobbe, J. C., Thiel, V., Ziebuhr, J., Poon, L. L., Guan, Y., Rozanov, M., Spaan, W. J. & Gorbalenya, A. E. (2003) *J. Mol. Biol.* **331,** 991–1004.
9. Thiel, V., Ivanov, K. A., Putics, A., Hertzig, T., Schelle, B., Bayer, S., Weissbrich, B., Snijder, E. J., Rabenau, H., Doerr, H. W., *et al.* (2003) *J. Gen. Virol.* **84,** 2305–2315.
10. Ziebuhr, J., Snijder, E. J. & Gorbalenya, A. E. (2000) *J. Gen. Virol.* **81,** 853–879.
11. Bost, A. G., Carnahan, R. H., Lu, X. T. & Denison, M. R. (2000) *J. Virol.* **74,** 3379–3387.
12. Campanacci, V., Egloff, M. P., Longhi, S., Ferron, F., Rancurel, C., Salomoni, A., Durousseau, C., Tocque, F., Brémond, N., Dobbe, J. C., *et al.* (2003) *Acta Crystallogr. D* **59,** 1628–1631.
13. Dauter, Z., Dauter, M. & Dodson, E. (2002) *Acta Crystallogr. D* **58,** 494–506.
14. Collaborative Computational Project 4 (1994) *Acta Crystallogr. D* **50,** 760–763.
15. Terwilliger, T. C. & Berendzen, J. (1999) *Acta Crystallogr. D* **55,** 849–861.
16. Terwilliger, T. C. (2002) *Acta Crystallogr. D* **58,** 1937–1940.
17. Roussel, A. & Cambillau, C. (1991) *Silicon Graphics Directory* (Silicon Graphics, Mountain View, CA).
18. Murshudov, G. N., Vagin, A. A. & Dodson, E. J. (1997) *Acta Crystallogr. D* **53,** 240–255.
19. Vaguine, A. A., Richelle, J. & Wodak, S. J. (1999) *Acta Crystallogr. D* **55,** 191–205.
20. Nicholls, A., Sharp, K. A. & Honig, B. (1991) *Proteins* **11,** 281–296.
21. Guex, N. & Peitsch, M. C. (1997) *Electrophoresis* **18,** 2714–2723.
22. Kraulis, P. J. (1991) *J. Appl. Crystallogr.* **24,** 946–950.
23. Merritt, E. A. & Bacon, D. J. (1997) *Methods Enzymol.* **277,** 505–524.
24. Gouet, P., Courcelle, E., Stuart, D. I. & Metoz, F. (1999) *Bioinformatics* **15,** 305–308.
25. Janin, J. & Rodier, F. (1995) *Proteins* **23,** 580–587.
26. Altschul, S. F. & Koonin, E. V. (1998) *Trends Biochem. Sci.* **23,** 444–447.
27. Holm, L. & Sander, C. (1995) *Trends Biochem. Sci.* **20,** 478–480.
28. Orengo, C. A., Michie, A. D., Jones, S., Jones, D. T., Swindells, M. B. & Thornton, J. M. (1997) *Structure (London)* **5,** 1093–1108.
29. Murzin, A. G., Brenner, S. E., Hubbard, T. & Chothia, C. (1995) *J. Mol. Biol.* **247,** 536–540.
30. Gutmann, S., Haebel, P. W., Metzinger, L., Sutter, M., Felden, B. & Ban, N. (2003) *Nature* **424,** 699–703.
31. Nissen, P., Kjeldgaard, M., Thirup, S., Clark, B. F. & Nyborg, J. (1996) *Biochimie* **78,** 921–933.
32. Arcus, V. (2002) *Curr. Opin. Struct. Biol.* **12,** 794–801.
33. Bochkarev, A., Bochkareva, E., Frappier, L. & Edwards, A. M. (1999) *EMBO J.* **18,** 4498–4504.
34. Bochkareva, E., Korolev, S., Lees-Miller, S. P. & Bochkarev, A. (2002) *EMBO J.* **21,** 1855–1863.
35. Seybert, A., Hegyi, A., Siddell, S. G. & Ziebuhr, J. (2000) *RNA* **6,** 1056–1068.
36. Brierley, I., Boursnell, M. E., Binns, M. M., Bilimoria, B., Blok, V. C., Brown, T. D. & Inglis, S. C. (1987) *EMBO J.* **6,** 3779–3785.
37. Kim, Y. T., Tabor, S., Bortner, C., Griffith, J. D. & Richardson, C. C. (1992) *J. Biol. Chem.* **267,** 15022–15031.
38. Kong, D. & Richardson, C. C. (1996) *EMBO J.* **15,** 2010–2019.
39. Kong, D., Nossal, N. G. & Richardson, C. C. (1997) *J. Biol. Chem.* **272,** 8380–8387.
40. Glassberg, J., Meyer, R. R. & Kornberg, A. (1979) *J. Bacteriol.* **140,** 14–19.